

Efficient Reverse Genetics Reveals Genetic Determinants of Budding and Fusogenic Differences between Nipah and Hendra Viruses and Enables Real-Time Monitoring of Viral Spread in Small Animal Models of Henipavirus Infection

Tatyana Yun,^{a,b} Arnold Park,^{f,g} Terence E. Hill,^{a,b} Olivier Pernet,^f Shannon M. Beaty,^{f,g} Terry L. Juelich,^{a,b} Jennifer K. Smith,^{a,b} Lihong Zhang,^{a,b} Yao E. Wang,^f Frederic Vigant,^{f,g} Junling Gao,^e Ping Wu,^e Benhur Lee,^{f,g} Alexander N. Freiberg^{a,b,c,d}

Department of Pathology,^a Galveston National Laboratory,^b Center for Biodefense and Emerging Infectious Diseases,^c Institute for Human Infections and Immunity,^d and Department of Neuroscience and Cell Biology,^e University of Texas Medical Branch, Galveston, Texas, USA; Department of Microbiology, Immunology and Molecular Genetics, University of California—Los Angeles, Los Angeles, California, USA^f; Department of Microbiology, Icahn School of Medicine at Mount Sinai, New York, New York, USA^g

ABSTRACT

Nipah virus (NiV) and Hendra virus (HeV) are closely related henipaviruses of the *Paramyxovirinae*. Spillover from their fruit bat reservoirs can cause severe disease in humans and livestock. Despite their high sequence similarity, NiV and HeV exhibit apparent differences in receptor and tissue tropism, envelope-mediated fusogenicity, replicative fitness, and other pathophysiologic manifestations. To investigate the molecular basis for these differences, we first established a highly efficient reverse genetics system that increased rescue titers by ≥ 3 log units, which offset the difficulty of generating multiple recombinants under constraining biosafety level 4 (BSL-4) conditions. We then replaced, singly and in combination, the matrix (M), fusion (F), and attachment glycoprotein (G) genes in mCherry-expressing recombinant NiV (rNiV) with their HeV counterparts. These chimeric but isogenic rNiVs replicated well in primary human endothelial and neuronal cells, indicating efficient heterotypic complementation. The determinants of budding efficiency, fusogenicity, and replicative fitness were dissociable: HeV-M budded more efficiently than NiV-M, accounting for the higher replicative titers of HeV-M-bearing chimeras at early times, while the enhanced fusogenicity of NiV-G-bearing chimeras did not correlate with increased replicative fitness. Furthermore, to facilitate spatiotemporal studies on henipavirus pathogenesis, we generated a firefly luciferase-expressing NiV and monitored virus replication and spread in infected interferon alpha/beta receptor knockout mice via bioluminescence imaging. While intraperitoneal inoculation resulted in neuroinvasion following systemic spread and replication in the respiratory tract, intranasal inoculation resulted in confined spread to regions corresponding to olfactory bulbs and salivary glands before subsequent neuroinvasion. This optimized henipavirus reverse genetics system will facilitate future investigations into the growing numbers of novel henipavirus-like viruses.

IMPORTANCE

Nipah virus (NiV) and Hendra virus (HeV) are recently emergent zoonotic and highly lethal pathogens with pandemic potential. Although differences have been observed between NiV and HeV replication and pathogenesis, the molecular basis for these differences has not been examined. In this study, we established a highly efficient system to reverse engineer changes into replication-competent NiV and HeV, which facilitated the generation of reporter-expressing viruses and recombinant NiV-HeV chimeras with substitutions in the genes responsible for viral exit (the M gene, critical for assembly and budding) and viral entry (the G [attachment] and F [fusion] genes). These chimeras revealed differences in the budding and fusogenic properties of the M and G proteins, respectively, which help explain previously observed differences between NiV and HeV. Finally, to facilitate future *in vivo* studies, we monitored the replication and spread of a bioluminescent reporter-expressing NiV in susceptible mice; this is the first time such *in vivo* imaging has been performed under BSL-4 conditions.

Nipah virus (NiV) and the closely related Hendra virus (HeV) are recently emergent, highly pathogenic paramyxoviruses that have the ability to cause severe and often fatal infections in humans and livestock, with clinical manifestations including acute febrile encephalitis and pulmonary syndromes. NiV has caused hundreds of cases in recurrent outbreaks in Southeast Asia, with high case fatality rates (ranging from 40 to 100%) (1), and 4 of 7 documented cases of HeV in Australia were fatal (2). These zoonotic viruses have repeatedly spilled over from their animal reservoir, *Pteropus* sp. fruit bats, either directly (i.e., through consumption of raw date palm sap contaminated with NiV-containing fluids) or via a domestic-animal intermediate (i.e., pigs for

NiV, or horses for HeV) (3). Because of their extreme pathogenicity and the absence of licensed human vaccines and antiviral therapeutics, the handling of henipaviruses is restricted to high-containment biosafety level 4 (BSL-4) laboratories.

Until recently, NiV and HeV were the sole known members of the *Henipavirus* genus within the *Paramyxoviridae*, a family of RNA viruses with negative-sense, nonsegmented genomes. In the past 2 years, examination of bats within and beyond the *Pteropus* genus has uncovered a multitude of previously undescribed henipaviruses of unknown virulence and implications for human health (4–7). The more widespread prevalence of henipaviruses and the documented human-to-human transmission of some

strains (8–10), along with recent evidence of potential henipavirus-like spillover events in Africa (11), suggest that increased global surveillance efforts directed at detecting henipavirus spillover events are warranted. Indeed, pandemic potential has been proposed for NiV (12). These findings underscore the urgency of understanding the molecular determinants of henipavirus pathogenesis and transmission.

NiV and HeV infections cause similar disease symptoms and pathology; it appears that virus transmitted through the oronasal-oropharyngeal routes leads to systemic infection that results in end-organ vasculitis, respiratory distress, and acute encephalitis (13). Both viruses use the highly conserved ephrin-B2 and -B3 receptor tyrosine kinases as host cell entry receptors, which explains their common preferential tropism for the vascular endothelium, lungs, and brain, all of which express high levels of cellular receptors (14). Although the paucity of known human cases of HeV infection makes it difficult to compare NiV and HeV, case histories suggest that HeV is difficult to contract, despite extensive exposure to infected aerosols and fluids from sick horses (3, 15). In contrast, the history of NiV outbreaks in Southeast Asia suggests that NiV may be easier to contract than HeV, and human-to-human transmission is clearly documented in Bangladesh as well (reviewed in reference 3).

Although NiV and HeV present grossly similar outcomes in human cases and established animal models (13, 16, 17), the few studies that have directly compared NiV and HeV replication and pathogenesis *in vitro* and *in vivo* have shown significant but variable differences (18–20) depending on the animal model used.

In the Syrian golden hamster model, intranasal (i.n.) inoculation revealed that HeV infection was restricted to the lower airways, whereas NiV could also replicate in the upper respiratory tract (19). However, HeV infection induced lesions and disseminated more quickly than NiV, leading to faster progression of encephalitic disease. Interestingly, some strains of aged immunocompetent mice also appeared to be more susceptible to HeV-induced encephalitis, whereas NiV infection resulted in only limited subclinical infection of the lungs (21, 22). In contrast, interferon alpha/beta receptor knockout (IFNAR KO) mice did not develop clinical signs of disease upon i.n. inoculation with HeV, although they were clearly susceptible to NiV infection via the same route (20). The IFNAR KO mouse results suggest that the anti-innate immune functions of the phosphoprotein gene and its associated alternative gene products cannot account for the differ-

ential pathology caused by HeV and NiV. Instead, differences in the matrix, fusion, and attachment proteins that can influence viral replication, tissue tropism, and the efficiency of viral entry might play a role in the pathogenic differences between HeV and NiV. Indeed, HeV may not use ephrin-B2 and/or ephrin-B3 as efficiently as NiV (23, 24). However, these putative differences attributable to the envelope attachment glycoprotein have not been appropriately examined in the context of a replication-competent virus.

To identify the molecular determinants contributing to the differences in pathobiology between NiV and HeV, we used reverse genetics to engineer chimeric NiVs in which the matrix and surface envelope genes were replaced by their HeV counterparts, either singly or in combination. To construct such a large panel of chimeras, we first took steps to improve the robustness and efficiency of viral rescue, critical considerations for work performed under BSL-4 conditions. A combination of technical strategies allowed for a pure transfection protocol that resulted in a 3-log-unit increase in viral rescue titers. We used this improved system to rescue recombinant NiV (Malaysia strain), HeV (prototype strain), and a panel of isogenic chimeras, each expressing an mCherry reporter. *In vitro* characterization revealed previously unknown differences in the budding and fusion properties of the henipavirus matrix protein and envelope glycoproteins, respectively. Finally, we also engineered a recombinant NiV expressing firefly luciferase (Fluc), which is suitable for *in vivo* bioluminescence imaging. Using the recently published IFNAR KO mouse model, we were able to monitor incipient and ongoing viral spread *in vivo*.

MATERIALS AND METHODS

Cells and viruses. Vero E6 cells (CRL1586; ATCC), Vero cells (CCL-81; ATCC), permissive HeLa cells (CCL-2; ATCC), 293T cells, and BSR-T7 cells (25) were propagated in Dulbecco's modified Eagle's medium (DMEM; Gibco, Invitrogen) supplemented with 10% fetal bovine serum (FBS; Sigma), 100 U/ml penicillin (Sigma), 100 µg/ml streptomycin (Sigma) and 1% sodium pyruvate (Cellgro). BSR-T7 cells were also maintained in 1 mg/ml G418. Virus-infected cells were maintained at 37°C under 5% CO₂ in DMEM supplemented with 2% FBS, 100 U/ml penicillin, and 100 µg/ml streptomycin. Human umbilical vein endothelial cells (HUVECs; Lonza) were maintained in EGM-2-MV medium (Lonza) supplemented with 2% FBS, hydrocortisone, human epidermal growth factor, gentamicin, amphotericin B, vascular endothelial growth factor, human fibroblast growth factor, fibroblast growth factor basic, R3 insulin-like growth factor 1, ascorbic acid, and heparin, provided through the EGM-2 BulletKit. For human fetal brain neural stem cells (NSCs), the K048 cell line (generously provided by C. N. Svendsen) was utilized as described previously (26).

Nipah virus (199901924 Malaysia prototype strain) was kindly provided by the Special Pathogens Branch (Centers for Disease Control and Prevention, Atlanta, GA, USA), and Hendra virus (prototype strain) was kindly provided by the Special Pathogens Program, National Microbiology Laboratory, Canadian Science Centre for Human and Animal Health (Winnipeg, Canada). The Nipah virus used in this study had been passaged a total of six times in Vero cells, and the Hendra virus was passaged four times in Vero cells. Viral stocks were prepared by infecting Vero E6 cells. For titrations, confluent monolayers of Vero cells were infected with 100 µl of serial 10-fold dilutions of virus-containing cell supernatant. After 1 h of incubation at 37°C under 5% CO₂, the inocula were removed, and wells were overlaid with a mixture of one part 1.0% methylcellulose (Fisher Scientific) and one part 2× MEM (Gibco) supplemented with 2% FBS and 2% penicillin-streptomycin. The plates were incubated at 37°C under 5% CO₂ for 3 days and were then stained with 0.25% crystal violet

Received 8 September 2014 Accepted 31 October 2014

Accepted manuscript posted online 12 November 2014

Citation Yun T, Park A, Hill TE, Pernet O, Beaty SM, Juelich TL, Smith JK, Zhang L, Wang YE, Vigant F, Gao J, Wu P, Lee B, Freiberg AN. 2015. Efficient reverse genetics reveals genetic determinants of budding and fusogenic differences between Nipah and Hendra viruses and enables real-time monitoring of viral spread in small animal models of henipavirus infection. *J Virol* 89:1242–1253. doi:10.1128/JVI.02583-14.

Editor: D. S. Lyles

Address correspondence to Benhur Lee, Benhur.Lee@mssm.edu, or Alexander N. Freiberg, anfreibe@utmb.edu.

T.Y. and A.P. contributed equally to this article.

Copyright © 2015, American Society for Microbiology. All Rights Reserved.

doi:10.1128/JVI.02583-14

TABLE 1 Henipavirus reverse genetics constructs

Name of antigenomic construct	Abbreviated name	Descriptive nomenclature ^{a,b}	T7 promoter
rNiV _{noG} -mCherry-P2A-M	rNiV _{noG} -mCh ^M	[NiV _{Mal}] T7 _{P-min} (mCherry-P2A-M)	TAATACGACTCACTATA
rNiV _{3G} -mCherry-P2A-M	rNiV _{3G} -mCh ^M	[NiV _{Mal}] T7 _{P-3G} (mCherry-P2A-M)	TAATACGACTCACTATAGGG
rNiV _{RbZA} -mCherry-P2A-M	rNiV-mCh ^M	[NiV _{Mal}] T7 _{P-3G(+)} 5' RbZA-(mCherry-P2A-M)	TAATACGACTCACTATAGGGAGA
rNiV _{RbZF} -mCherry-P2A-M	rNiV _{RbZF} -mCh ^M	[NiV _{Mal}] T7 _{P-3G} 5' RbZF-(mCherry-P2A-M)	TAATACGACTCACTATAGGG
rNiV _{RbZA} -mCherry-P2A-M: HeV-M	rNiV-mCh ^M -HeV-M	[NiV _{Mal}] T7 _{P-3G(+)} 5' RbZA-(mCherry-P2A-M) ¹ -(M → M _{HeV-Aus}) ²	TAATACGACTCACTATAGGGAGA
rNiV _{RbZA} -mCherry-P2A-M: HeV-F	rNiV-mCh ^M -HeV-F	[NiV _{Mal}] T7 _{P-3G(+)} 5' RbZA-(mCherry-P2A-M) ¹ -(F → F _{HeV-Aus}) ²	TAATACGACTCACTATAGGGAGA
rNiV _{RbZA} -mCherry-P2A-M: HeV-G	rNiV-mCh ^M -HeV-G	[NiV _{Mal}] T7 _{P-3G(+)} 5' RbZA-(mCherry-P2A-M) ¹ -(G → G _{HeV-Aus}) ²	TAATACGACTCACTATAGGGAGA
rNiV _{RbZA} -mCherry-P2A-M: HeV-F/G	rNiV-mCh ^M -HeV-F/G	[NiV _{Mal}] T7 _{P-3G(+)} 5' RbZA-(mCherry-P2A-M) ¹ -(F/G → F/G _{HeV-Aus}) ²	TAATACGACTCACTATAGGGAGA
rNiV _{RbZA} -mCherry-P2A-M: HeV-M/F/G	rNiV-mCh ^M -HeV-M/F/G	[NiV _{Mal}] T7 _{P-3G(+)} 5' RbZA-(mCherry-P2A-M) ¹ -(M/F/G → M/F/G _{HeV-Aus}) ²	TAATACGACTCACTATAGGGAGA
rNiV _{RbZA} -N-EGFP _P	rNiV-EGFP ^{NP}	[NiV _{Mal}] T7 _{P-3G(+)} 5' RbZA-(N-EGFP _P)	TAATACGACTCACTATAGGGAGA
rNiV _{RbZA} -N-Fluc _P	rNiV-Fluc ^{NP}	[NiV _{Mal}] T7 _{P-3G(+)} 5' RbZA-(N-Fluc _P)	TAATACGACTCACTATAGGGAGA
rHeV _{RbZA} -mCherry-P2A-M	rHeV-mCh ^M	[HeV _{Aus}] T7 _{P-3G(+)} 5' RbZA-(mCherry-P2A-M)	TAATACGACTCACTATAGGGAGA

^a The virus and strain (subscript; Mal, Malaysian; Aus, Australian) are given in square brackets, followed by the type of promoter, the type of 5' HHRbz, if any, and major features (within parentheses). Where there is more than one feature, each is labeled with a superscript number. Within a feature, "-" indicates a direct connection (e.g., mCherry-P2A-M), whereas "-" indicates the context (e.g., N-EGFP_P).

^b T7_{P-min} is the minimal T7 promoter without additional G's to drive higher levels of transcription; T7_{P-3G} has 3 additional G's to drive higher levels of transcription; and T7_{P-3G(+)} has an additional AGA sequence that is part of the optimal T7 promoter.

in 10% buffered formalin. Plates were washed, plaques enumerated, and viral titers (PFU/ml) in the cell culture supernatant calculated. All work with live virus was carried out under biosafety level 4 conditions in the Robert E. Shope Laboratory and the Galveston National Laboratory at the University of Texas Medical Branch (UTMB).

Ribozyme cleavage assay. Ribozyme test constructs (see Fig. 1B), inserted between the NdeI and HindIII sites in pcDNA3.1(-), were transfected into BSR-T7 cells in a 6-well format using Lipofectamine 2000 (Invitrogen). The hammerhead ribozyme (HHRbz) sequences tested were derived and modified from a number of publications (27–32) as indicated in Fig. 1A. Two hours posttransfection, cells were collected in TRIzol (Invitrogen), and RNA was extracted according to the manufacturer's instructions. Samples were treated with DNase (Invitrogen) at 1 mM MgCl₂, treated with EDTA, and then reverse transcribed at 1 mM MgCl₂ with the SuperScript III First-Strand Synthesis system (Invitrogen). Quantitative PCR (qPCR) was performed with the SensiFAST SYBR & Fluorescein kit (Bioline), and the primers used were positioned as indicated in Fig. 1B (sequences are available on request). Standard curves were generated by using the RbZA test construct as the template.

Construction of rNiV_{RbZA}-mCherry-P2A-M. A list of the constructs in this study, with explanations of the nomenclature, is provided in Table 1. A T7-driven positive-sense NiV "minigenome," between the NdeI and HindIII restriction sites in pcDNA3.1(-), was previously synthesized with the following elements: T7 promoter, 3' leader, N 5' untranslated region (UTR), red fluorescent protein (RFP), N 3' UTR, M 5' UTR, M, M 3' UTR, F 5' UTR, F, F 3' UTR, G 5' UTR, G, G 3' UTR, 5' trailer, hepatitis delta virus (HDV) ribozyme, and T7 terminator. NiV-N, -P, and -L were amplified from the pTM1-based accessory plasmids described previously (33). The P and L 5' and 3' UTRs were synthesized by GenScript. The full-length construct displayed in Fig. 2A was assembled by serial modification of the original minigenome construct by use of overlapping PCRs to join DNA fragments with Velocity DNA polymerase (Bioline), with subsequent insertion into the construct at unique restriction sites by restriction digestion/ligation or In-Fusion cloning (Clontech). All cloning was performed with *Escherichia coli* Stbl2 (Invitrogen) with growth at 30°C. The NiV sequence matches NCBI accession no. NC_002728.1 except for one silent mutation in N, A649G (numbered according to the position in the NCBI sequence).

Subsequent modifications to rNiV. All mutagenesis and modification were performed using standard overlapping PCR with Velocity DNA polymerase (Bioline); the ends of the final DNA product were compatible with the use of In-Fusion cloning (Clontech) for insertion into the desired restriction sites in recombinant NiV (rNiV). Existing restriction sites were sufficient; it was not necessary to introduce artificial restriction sites (except for a single introduced site usually flanking the 3' end of the reporter gene for cloning convenience). Insertion into digested rNiV was performed by restriction digestion/ligation or In-Fusion cloning (Clontech). The ligation or In-Fusion reaction product was transformed into Stbl2 cells (Invitrogen) and was selected on LB ampicillin at 30°C overnight. Clones were grown in Terrific broth (TB) ampicillin at 30°C, screened by restriction digestion, and fully sequenced. For the construction of the rNiV-HeV chimeras, the HeV-M, -F, and -G open reading frames (ORFs) were amplified from HeV cDNA (see below) and were used to replace the corresponding NiV genes in rNiV_{RbZA}-mCherry-P2A-M in various combinations (see Fig. 2A). For the construction of rNiV-EGFP^{NP} and rNiV-Fluc^{NP}, the enhanced green fluorescent protein (EGFP) and firefly luciferase (Fluc) ORFs were inserted between the N and P genes, with duplication of the N-to-P intergenic region.

Construction of rHeV_{RbZA}-mCherry-P2A-M. Positive-sense cDNA was amplified from HeV prototype strain (GenBank accession no. AF017149) RNA using the AccuScript High Fidelity 1st Strand cDNA synthesis kit (Agilent). DNA fragments were amplified from cDNA using Velocity DNA polymerase (Bioline) and were cloned into rNiV_{RbZA}-mCherry-P2A-M-(HeV-M/F/G) by serial replacement, first between MluI and NotI, then between NotI and AgeI, and finally, with simultaneous insertion of two fragments, between AgeI and PmeI using In-Fusion cloning (Clontech). The HHRbz sequence in stem I designed to anneal to the NiV 3' leader, TTGGT, was mutated to TCGGT so as to match the HeV 3' leader. For the support plasmids, HeV-N, -P, and -L were cloned into pTM1 as described previously for NiV (33), with the two C ORF start codons mutated in P (from ATGATG to ACGACG) to prevent potential inhibition of rescue (34).

Recovery of recombinant viruses from cDNA. The procedure for the recovery of recombinant viruses was slightly modified from previously described protocols (35, 36). 293T cells were seeded into 12-well plates (1.5 × 10⁵ cells per well). Cells were transfected the following day with the

rNiV antigenomic construct (3.5 μ g), codon-optimized T7 RNA polymerase (RNAP) in pCAGGS (1 μ g), and the previously published support plasmids (33) encoding NiV-N (1 μ g), NiV-P (0.2 μ g), and NiV-L (0.4 μ g) by using the TransIT-LT1 transfection reagent (Mirus) according to the manufacturer's recommendations. After 4 days, syncytium formation and expression of fluorescent reporter genes could be detected by microscopy. Supernatants were collected at 4 days posttransfection and were stored at -80°C for subsequent preparation of virus stocks and determination of virus titers by plaque assays with Vero cells.

Virus growth kinetics. Cells in a 12-well format were infected at a multiplicity of infection (MOI) of 0.1 or 1, and supernatants were collected and replenished every 12 h postinfection (hpi). Samples were stored at -80°C until the determination of viral titers by plaque assays with Vero cells. The statistical significance of differences in virus growth kinetics was determined by two-way analysis of variance (ANOVA), with Bonferroni posttests to determine significance at each time point.

Immunofluorescence staining. HUVECs on coverslips were infected at an MOI of 0.1. At 24 hpi, cells were fixed with 10% formalin for a minimum of 24 h prior to removal from the BSL-4 laboratory. Samples were washed 3 times with phosphate-buffered saline (PBS), incubated for 15 min in blocking buffer (0.5% saponin, 3% bovine serum albumin [BSA] in PBS), and then incubated with Alexa Fluor 647 phalloidin (1:250; Invitrogen) in blocking buffer. After 3 washes with 0.5% saponin in PBS, samples were incubated with 4',6-diamidino-2-phenylindole (DAPI) to stain nuclei before mounting on slides. Confocal imaging was performed on a Leica SP5 confocal microscope. The statistical significance of differences in syncytium formation between HeV-G-bearing viruses and non-HeV-G-bearing viruses was determined by one-way ANOVA followed by a Tukey pairwise multiple-comparison test.

qPCR of transcriptional gradients. HUVECs were infected with wild-type NiV or rNiV-mCh^M at an MOI of 0.1. RNA was isolated from TRIzol (Invitrogen) samples collected 12 hpi. mRNAs were purified from total RNA by using the Dynabeads mRNA purification kit (Invitrogen) and were reverse transcribed into cDNA with oligo(dT) primers and the Tetro cDNA synthesis kit (Bioline). qPCR using the SensiFAST SYBR & Fluorescein kit (Bioline) was performed using gene-specific primers (sequences available on request), and standard curves for each gene were generated by a shared serial dilution of the full-length rNiV plasmid.

Immunoblotting. For comparison of NiV-M and HeV-M budding, the 3 \times FLAG-tagged codon-optimized matrix gene (37) in pCMV-3Tag-1A (Agilent) was transfected into 293T cells with the BioT transfection reagent (Bioline) according to the manufacturer's recommendations. The medium was changed at 4 h posttransfection (hpt), and cell lysates and supernatants were collected at 18 hpt. Supernatants were clarified and ultracentrifuged through 20% sucrose at $145,000 \times g$ for 1.5 h to pellet virus-like particles. Samples in SDS Laemmli buffer were boiled and were run on 10% Tris-glycine SDS-PAGE gels. Upon transfer to polyvinylidene difluoride (PVDF) membranes (Immobilon-FL; Millipore), the membranes were incubated in Odyssey blocking buffer (Li-Cor Biosciences) overnight at 4°C ; then they were incubated with mouse anti-FLAG antibody M2 (1:50,000; Stratagene) or a rabbit antibody against cytochrome *c* oxidase subunit 4 isoform 1, mitochondrial (COX IV) (1:2,000; Li-Cor Biosciences), for 1 h at room temperature, followed by a fluorescent secondary antibody (goat anti-mouse IRDye 800CW or goat anti-rabbit IRDye 680LT [1:10,000; Li-Cor Biosciences]). Fluorescence images were obtained on a Li-Cor Odyssey imaging system. The statistical significance of differences in budding efficiency was determined by a 2-tailed paired Student *t* test for 3 independent experiments.

In vivo imaging. Interferon alpha/beta receptor knockout (IFNAR KO) mice (5 to 7 weeks old; 129/Sv background; obtained from the laboratory colony of Slobodan Paessler at UTMB [38]) were utilized for bioluminescence imaging on an *in vivo* imaging system (IVIS) at BSL-4 containment. Prior to inoculation, mice were shaved to maximize detection of the bioluminescent signal. Mice were anesthetized with 2% isoflurane and were inoculated either with 8×10^5 PFU/100 μ l/mouse of rNiV-

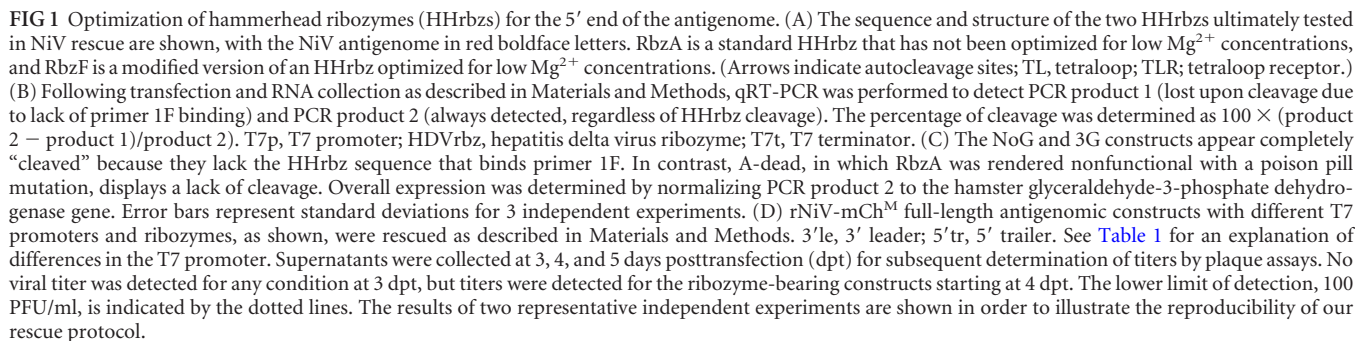
Fluc^{NP} via the intraperitoneal (i.p.) route or with 8×10^4 PFU/50 μ l/mouse via the intranasal (i.n.) route. Prior to imaging, mice were given D-luciferin (Caliper) through the i.p. route (150 mg/kg). Bioluminescence was measured using an IVIS Spectrum platform, which was equipped with a charge-coupled device (CCD) camera system. Images were analyzed with the Living Image software package, version 4.3.1. The acquisition time was set to "auto" for each image, with f/stop fixed at F1, and medium binning.

RESULTS

Improved henipavirus reverse genetics with an optimized self-cleaving hammerhead ribozyme. Paramyxovirus rescue systems typically incorporate a GGG sequence between the minimal T7 promoter and the 5' end of the antigenome, thus allowing relatively efficient transcription by T7 polymerase yet impeding efficient rescue, because the G's must be lost from the genomic transcript to maintain the rule of six and the appropriate terminal sequence. With the aim of improving the reliability and efficiency of reverse genetics for use under relatively onerous BSL-4 conditions, we evaluated whether the inclusion of a self-cleaving hammerhead ribozyme (HHrbz) at the 5' end of the antigenome would increase rescue efficiency by providing the exact genomic terminus required for efficient replication and thus allowing the inclusion of the transcript-initiating GGG sequence in the optimal T7 promoter. We modified and screened seven HHrbz motifs for cleavage efficiency at the 5' end of the NiV antigenome (Fig. 1A). RbzA represents a standard HHrbz, whereas the other HHrbzs are thought to retain efficient cleavage at the low magnesium concentrations reflective of the intracellular environment (submillimolar Mg^{2+} concentrations). Using a reverse transcription-quantitative PCR (qRT-PCR)-based assay to detect cleavage of RNA isolated from transfected cells (Fig. 1B), we found that three ribozymes (RbzD, RbzF, and RbzG) self-cleaved with an efficiency similar to, or greater than, that of RbzA; of these, RbzF resulted in essentially complete cleavage (Fig. 1C). Surprisingly, even RbzA, the standard HHrbz not optimized for low Mg^{2+} conditions, resulted in nearly 90% cleavage. We then chose to evaluate whether RbzA and RbzF would improve the rescue efficiency of full-length recombinant NiV.

We therefore constructed a full-length NiV cDNA (based on the Malaysia strain) with a T7-driven antigenome flanked at the 3' end by a hepatitis delta virus ribozyme, and we inserted an mCherry fluorescent reporter upstream of the matrix protein (M) gene, linked to M via a P2A ribosomal skipping sequence. As has been suggested previously, incorporating the reporter as part of an existing ORF may better preserve the natural polar transcriptional gradient of the virus (39). Four versions of the full-length cDNA were made, with either no additional G's (T7_{min}), 3 G's ($\text{T7}_{3\text{G}}$), RbzA [$\text{T7}_{3\text{G}(+)} \text{HH}_{\text{RbzA}}$], or RbzF [$\text{T7}_{3\text{G}} \text{HH}_{\text{RbzF}}$] following the minimal T7 promoter (Fig. 1D). These constructs were individually cotransfected with the essential support plasmids [codon-optimized T7 polymerase and T7-driven NiV nucleoprotein (N), phosphoprotein (P), and RNA-dependent RNA polymerase (L)] into 293T cells. Determination of the titers of cell culture supernatants collected 4 to 5 days posttransfection revealed that inclusion of RbzA, and to a lesser extent RbzF, resulted in a ≥ 3 -log increase in rescue viral titers over those for constructs without an HHrbz (Fig. 1D). We therefore chose to include RbzA in our future reverse genetics constructs.

Our rescue system was robust, as evidenced by the fact that $>80\%$ of the recombinant viruses we have successfully rescued



thus far in this study (Table 1) and previous work (see, e.g., reference 11) have been rescued on the first attempt (unpublished observations). Use of the codon-optimized T7-RNAP (T7opt) is critical: it obviates the need for vaccinia virus-driven T7-RNAP, which has unavoidable cytopathic effects, and it also removes the cryptic splice sites present in bacteriophage-derived T7-RNAP. This robust and efficient HHrbz-T7opt-based reverse genetics system enabled us to more readily generate multiple recombinant henipaviruses for studies on henipavirus replication and pathogenesis.

Recombinant NiV-HeV chimeras reveal that the henipavirus matrix and envelope proteins exhibit heterologous cross-complementation. To determine if the viral envelope fusion (F) and attachment (G) glycoproteins, as well as the matrix (M) protein, contribute to the differences reported in NiV and HeV infections, we generated a panel of chimeric henipaviruses in an isogenic rNiV_{RbZA}-mCherry-P2A-M (rNiV-mCh^M) background (Fig. 2A; see Table 1 for additional details). We replaced the M, F, and G genes in rNiV-mCh^M, singly or in combination, with their HeV counterparts. In addition, we generated the full-length recombinant HeV counterpart, rHeV_{RbZA}-mCherry-P2A-M (rHeV-mCh^M). All recombinant viruses were successfully rescued and replicated well, albeit to differing degrees, in primary human neuron/astrocyte cultures derived from fetal cortical neural stem cells (hNSC-derived neurons/astrocytes), as well as in primary human umbilical vein endothelial cells (HUVECs), plateauing at 36 to 48 hpi (Fig. 2B and C). As addressed further below, the recombinant rNiV-mCh^M and rHeV-mCh^M were significantly attenuated in comparison to the parental wild-type viruses (Fig. 2B and C, left).

The NiV and HeV F and G glycoproteins are known to functionally cross-complement each other in cell-cell fusion assays and viral pseudotype entry assays (23, 40), both of which require overexpression of the F and G genes. Whether such heterotypic envelope cross-complementation will occur in the context of a replication-competent virus has not been examined. Here, the efficient replication of the chimeras rNiV-mCh^M-HeV-F and rNiV-mCh^M-HeV-G (Fig. 2B and C, right) confirms that heterotypic complementation occurs in a biologically relevant context. Interestingly, we also found that the matrix proteins of NiV and HeV can support functional incorporation of the heterotypic envelope glycoproteins (rNiV-mCh^M-HeV-F/G and rNiV-mCh^M-HeV-M, respectively) (Fig. 2B and C, right). Further highlighting the genetic relatedness of NiV and HeV, the replication of rNiV-mCh^M-HeV-M also demonstrates that HeV-M, in its role as the central organizer of viral assembly and budding, can functionally interface with the heterotypic NiV N-P-L replication complex.

HeV-M buds more efficiently than NiV-M. Unexpectedly, at early time points (12 and 24 hpi) in both hNSC-derived neurons/astrocytes and HUVECs (Fig. 2B and C, right), the chimeras bearing either HeV-M or HeV-M/F/G replicated to significantly higher titers than the parental virus rNiV-mCh^M or any of the other chimeras lacking HeV-M. Quantitative Western blotting for matrix in a virus-like particle budding assay indicated that HeV-M buds about 2.5-fold more efficiently than NiV-M (Fig. 2D and E), providing a potential explanation for the increased titers seen for the HeV-M-bearing chimeras at early time points.

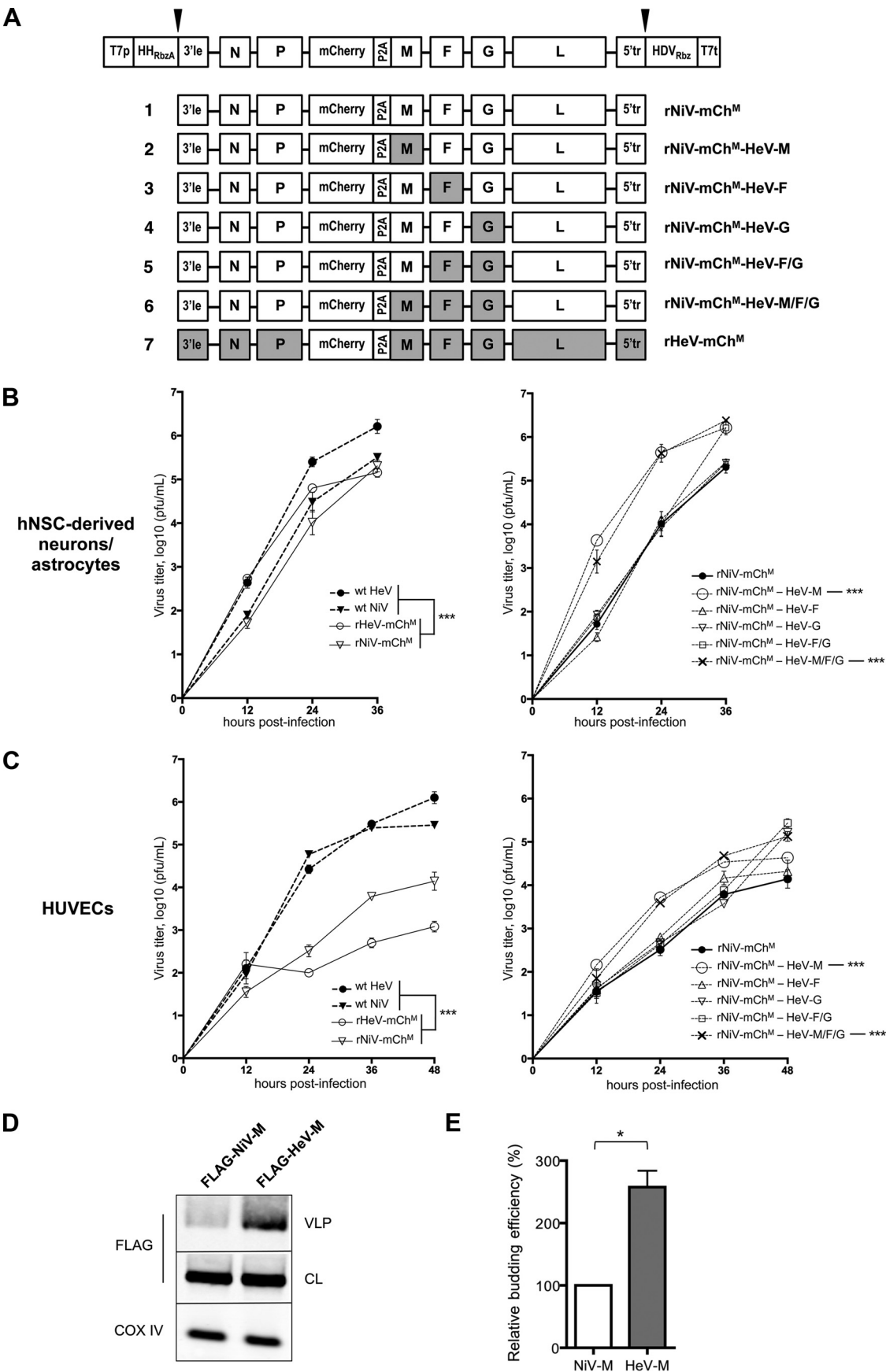
Fusogenicity is not a correlate of replicative fitness. Furthermore, our data show that the HeV-G-bearing viruses are less fusogenic than their NiV-G-bearing counterparts. The presence of HeV-G, whether in an rNiV-mCh^M chimera (constructs 4 to 6) or

in full-length recombinant HeV (rHeV-mCh^M; construct 7), resulted in less syncytium formation at 24 hpi than in viruses that expressed NiV-G (constructs 1 to 3) (Fig. 3A and B). In agreement with this observation, both viruses bearing homotypic NiV-F/G (constructs 1 and 2) exhibited more syncytium formation at 24 hpi than the viruses bearing homotypic HeV-F/G (constructs 5 to 7) (Fig. 3A and B). This differential fusogenicity was not an artifact of the recombinant genetic background used, as evidenced by the fact that nonrecombinant wild-type NiV also formed more numerous syncytia than wild-type HeV during infection of the same primary cell types (HUVECs) (data not shown). Yet despite this apparently greater fusogenicity of the NiV-F/G-bearing viruses, they plateaued at similar or lower titers than their isogenic HeV-F/G-bearing counterparts, suggesting that fusogenicity is not a correlate of replicative fitness, at least *in vitro* (Fig. 2B and C).

Insertion of an ORF between the N and P genes does not affect the NiV transcriptional gradient. In our initial chimeric constructs, we inserted the mCherry ORF upstream of the matrix gene via a P2A ribosomal skipping sequence to avoid disturbing the natural polar transcriptional gradient. Indeed, our quantitative comparison of viral mRNA transcripts upon infection with either wild-type NiV or rNiV-mCh^M showed similar transcriptional gradients: mRNA levels were stable for the first three genes (N, P, and M) but decreased exponentially thereafter, about 3-fold for each subsequent gene (Fig. 4A). The transcriptional gradient drop-off for HeV also occurs right after the M gene (41). Despite the similar transcriptional gradients for wild-type NiV and rNiV-mCh^M, we observed that rNiV-mCh^M had slower replication kinetics *in vitro*, in permissive cell lines, such as Vero cells (Fig. 4B), and in primary human cells, such as hNSC-derived neurons/astrocytes and HUVECs (Fig. 2B and C). Indeed, rHeV-mCh^M was similarly attenuated compared to wild-type HeV on these primary human cells.

While our mCherry-P2A-matrix reporter strategy was useful in revealing the differential determinants of budding and fusogenicity for NiV and HeV in isogenic comparisons *in vitro*, we sought a reporter insertion strategy that would more closely reflect wild-type NiV replication kinetics. We therefore rescued a recombinant NiV with EGFP inserted between the N and P genes, with duplication of the N-to-P intergenic region (rNiV-EGFP^{NP}) (Table 1), a strategy similar to that reported by Yoneda et al. (36). The transcriptional gradient of rNiV-EGFP^{NP} was similar to that of rNiV-mCh^M (Fig. 4A), but the *in vitro* growth of rNiV-EGFP^{NP} was now indistinguishable from that of wild-type NiV (Fig. 4B).

Fluc-expressing rNiV allows real-time monitoring of virus replication and spread in the IFNAR KO mouse. To our knowledge, henipavirus spread and pathogenesis has been examined only in autopsy series or in serial sacrifice studies of experimentally infected animals. To complement the future use of our NiV-HeV chimeras for examining the pathogenic symptomatology in animal models, we generated a firefly luciferase (Fluc)-expressing rNiV using the N-P intergenic insertion strategy described above (rNiV-Fluc^{NP}) (Table 1). Viral expression of the nonsecreted Fluc reporter would allow for real-time monitoring of bioluminescence at sites of viral replication. As expected, the growth of rNiV-Fluc^{NP} was similar to that of wild-type NiV in HUVECs (Fig. 5A). We then infected IFNAR KO mice (20) with rNiV-Fluc^{NP} and monitored the spatial and temporal progression of viral replication, as presented in Fig. 5. Two groups of IFNAR KO mice (two females and two males per group) were infected via the i.n. or i.p.



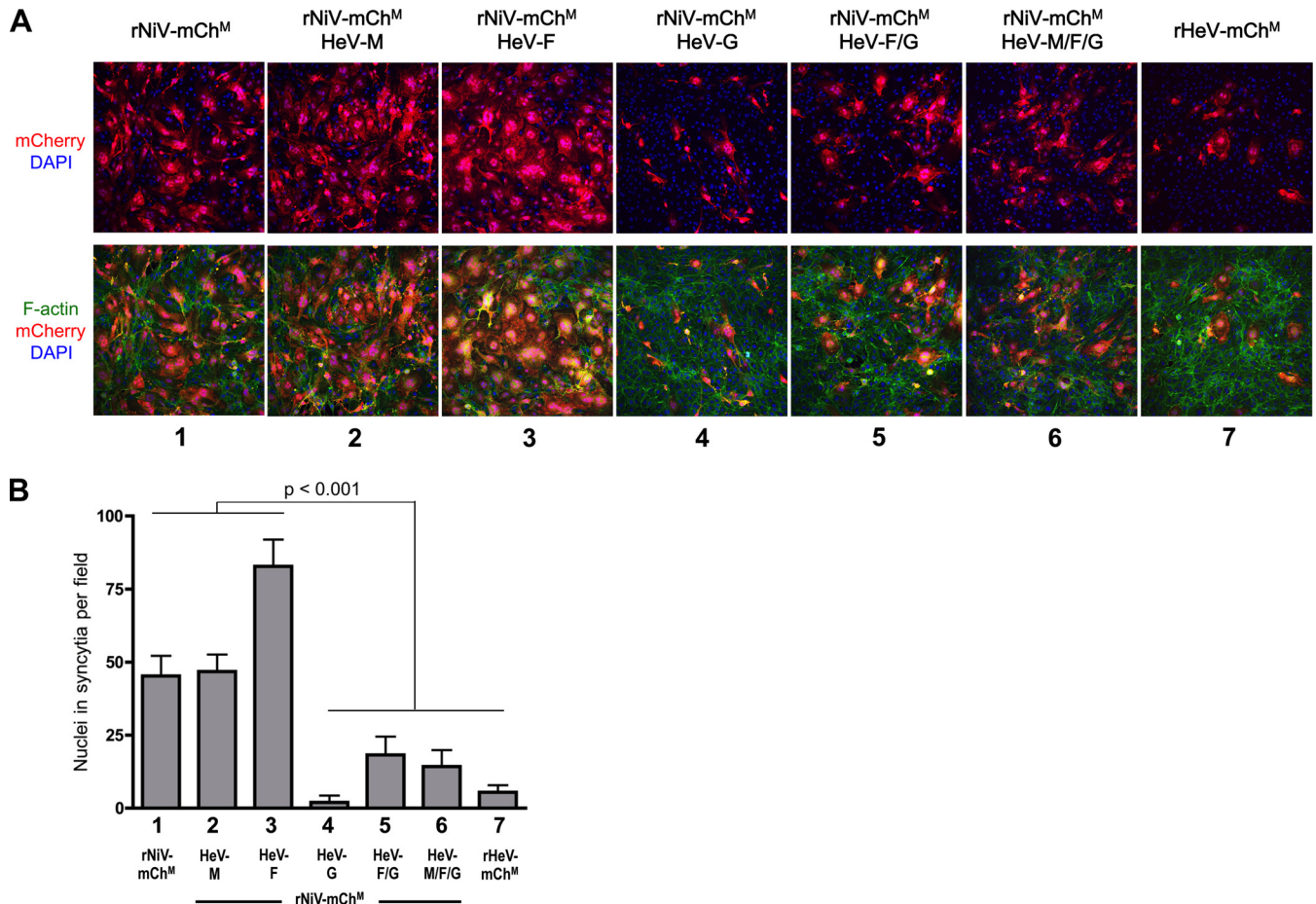


FIG 3 Fusogenicity of recombinant NiV-HeV chimeras in infected HUVECs. Immunofluorescence imaging of syncytium formation in infected HUVECs shows differential fusogenicity of recombinant NiV-HeV chimeras. (A) HUVECs on coverslips were infected with the indicated mCherry-expressing viruses at an MOI of 0.1. At 24 h postinfection, coverslips were fixed in formalin and were stained with DAPI (blue) (for nuclei) and Alexa Fluor 647 phalloidin (green) (for F-actin). Confocal z-stacks (magnification, $\times 20$) were obtained, and a representative extended-focus image for each virus is shown. Numbers below the images refer to the diagrams in Fig. 2A. (B) Nuclei within syncytia (3 or more nuclei within an mCherry-positive cell) were counted in 4 independent fields (magnification, $\times 40$) per virus. Error bars represent standard deviations. One-way ANOVA followed by a Tukey pairwise multiple-comparison test shows that all HeV-G-bearing viruses form significantly fewer syncytia than all NiV-G-bearing viruses ($P < 0.001$).

route, respectively, and mice were imaged daily starting at 2 days postinfection (dpi) using the *in vivo* imaging system (IVIS) at BSL-4.

Intranasal inoculation resulted in viral replication primarily confined to the upper respiratory tract (Fig. 5B). All peripheral

organs in the i.n.-infected group lacked luminescence signals throughout the duration of the study, except for a transient, weak signal in the spleens of three out of four mice at 4 dpi. Interestingly, serial sacrifice studies of NiV-infected Syrian golden hamsters (19) also detected transient viral replication in the spleen.

FIG 2 Replication kinetics of rNiV-HeV chimeras reveals heterologous cross-complementation of henipavirus matrix and envelope proteins and demonstrates that HeV-M buds more efficiently than NiV-M. (A) The parental rNiV-mCh^M construct and relevant rNiV-HeV chimeras generated and rescued in this study are schematically diagrammed. Genetic components from HeV are shaded. T7p, T7 promoter; 3'le, 3' leader; 5'tr, 5' trailer; T7t, T7 terminator. The arrowheads indicate where the hammerhead ribozyme (HH_{Rbz}) and hepatitis delta virus ribozyme (HDV_{Rbz}) self-cleave. (B and C) hNSC-derived neurons/astrocytes (B) and HUVECs (C) were infected with the indicated wild-type (wt) and recombinant viruses at an MOI of 0.1, and the growth kinetics were monitored as described in Materials and Methods. Results of representative experiments are shown. Error bars represent standard deviations for triplicate samples. Two-way ANOVA followed by Bonferroni posttests shows that both rNiV-mCh^M and rHeV-mCh^M are significantly attenuated compared to their respective wild-type parental viruses (left) at 24 hpi in both hNSC-derived neurons/astrocytes and HUVECs ($***$, $P < 0.001$). The same analysis shows that both HeV-M-bearing chimeras have significantly higher titers than all NiV-M-bearing rNiVs (right) at 24 hpi in both hNSC-derived neurons/astrocytes and HUVECs ($***$, $P < 0.001$). (D and E) HeV-M buds more efficiently than NiV-M. (D) FLAG-tagged NiV-M and HeV-M were transfected into 293T cells. Eighteen hours posttransfection, cell lysates (CL) and virus-like particles (VLP) in supernatants were collected and were Western blotted for the matrix protein (anti-FLAG) as described in Materials and Methods. A representative comparison of NiV-M with HeV-M in CL and VLP is shown. COX IV was used as the cell lysate loading control. (E) For each experiment, titrated NiV-M was transfected to determine a best-fit NiV-M budding curve of the relative amount of the matrix protein in CL (x variable) versus the relative amount of the matrix protein in VLP (y variable), as determined by quantitative fluorescent Western blotting. In the same experiment, the relative budding efficiency of HeV-M was determined by comparison to this best-fit NiV-M budding curve. The error bar represents the standard deviation for 3 independent experiments; the asterisk indicates a significant difference ($P = 0.0265$) by a 2-tailed paired Student t test.

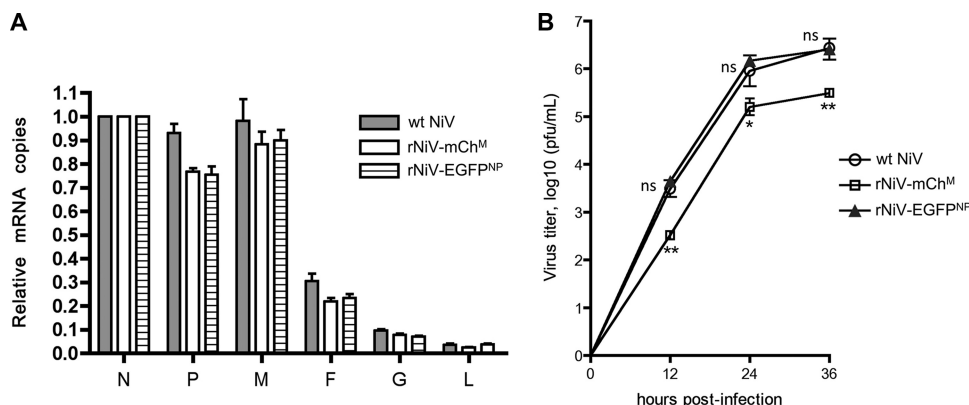


FIG 4 Insertion of an ORF between the N and P genes does not affect the NiV transcriptional gradient. (A) Wild-type (wt) and recombinant NiVs have similar transcriptional gradients. HUVECs were infected with the indicated viruses at an MOI of 0.1, and RNA was isolated from samples collected at 24 hpi. mRNAs were selectively purified using oligo(dT) magnetic beads. qRT-PCR was performed for the viral genes, and standard curves were generated by a shared serial dilution of the full-length rNiV plasmid. Error bars represent standard deviations for 3 independent experiments. (B) Vero cells were infected with the indicated viruses at an MOI of 1, and the growth kinetics were monitored as described in Materials and Methods. Error bars represent standard deviations for 3 replicates. Two-way ANOVA followed by Bonferroni posttests was used to examine the significance of differences from wt NiV (*, $P < 0.05$; **, $P < 0.01$; ns, not significant).

Bioluminescence remained confined to the oropharyngeal/oronasal areas at 3 to 5 dpi, including regions anatomically consistent with the location of the major salivary glands. In mice, the bilateral submandibular, sublingual, and parotid glands form a contiguous structure across the anterior and lateral neck (42). Mice presented with hunched posture at 6 and 7 dpi, consistent with bioluminescence signals observed in the central nervous system (CNS), but half the mice survived until the end of the study at 21 dpi with no overt symptoms.

In contrast, i.p. inoculation resulted in systemic infection by 2 dpi, as indicated by low levels of bioluminescence throughout the main body cavity (Fig. 5C, bottom), with virus replication (bioluminescence) highest in the spleen (Fig. 5C, top). At 3 to 4 dpi, NiV progressively spread to the lungs, the respiratory tract, and nasal turbinates. By 5 to 6 dpi, increasing bioluminescence in the olfactory bulb and invasion of the brain were obvious, coinciding with the development of clinical signs of disease, such as hunched posture, hyperreflexia, lethargy, seizures, and ataxic behavior.

These results expand on the report by Dhondt et al. (20) by providing evidence that even with i.p. infection in this animal model, invasion of the brain may result at least in part from respiratory transmission to the olfactory bulb. All i.p.-inoculated mice developed robust infections and were euthanized between days 6 and 8 postinfection. Mice that were moribund after i.p. infection exhibited luminescence signals in the upper respiratory tract (including regions of the salivary glands) and urinary tract (kidneys and bladder) (Fig. 5C, day 6, bottom), in agreement with presumed modes of henipavirus transmission via saliva and urine. *Ex vivo* imaging of fresh, nonfixed whole brains from moribund mice after i.p. infection revealed viral replication in the olfactory bulb, olfactory tubercle, frontal cortex, and cerebellum (Fig. 5D). Coronal brain slices further revealed bioluminescence signals in deeper brain structures, such as the olfactory nucleus, anterior commissure, nucleus accumbens, basal forebrain, and amygdala nuclei (Fig. 5E).

Taken together, these data demonstrate the usefulness of Fluc-expressing henipaviruses in enabling sensitive detection and identification of early replication sites, as well as monitoring of the spread and development of disease, with the ultimate goal of iden-

tifying the molecular determinants of henipavirus-induced pneumonia and encephalitis.

DISCUSSION

Reverse genetics systems for *Mononegavirales*, or the viruses with negative-sense, nonsegmented RNA genomes, have typically been fraught with inefficiency (43), and BSL-4 conditions make their use even more difficult. The addition of a hammerhead ribozyme between the optimal T7 promoter and the 5' end of the anti-genome has been shown to improve rescue for certain negative-strand RNA viruses, such as rabies virus (44), and we demonstrate here that this strategy also significantly improves rescue for henipaviruses. While Lo et al. (39) recently reported the rescue of NiV by using an HHrbz, it is not clear whether (or by how much) the inclusion of their HHrbz improves rescue, because no comparative data on the rescue efficiencies achieved was reported. In light of the known sequence-dependent efficiency of ribozyme cleavage (45), we screened seven HHrbz designs, three of which cleaved at efficiencies equivalent to, or better than, that of the "standard" RbzA. These other HHrbz designs may be useful in a sequence-dependent context for the rescue of other negative-sense RNA viruses that require exact 5' and 3' termini.

Additionally, we also developed a one-step transfection protocol using a custom-designed codon-optimized T7 RNA polymerase expression plasmid, rather than recombinant vaccinia virus, as the source for T7 polymerase. A vaccinia virus-free rescue system alleviates the cytopathic effect and other technical complications associated with vaccinia virus infections, such as blind passaging on vaccinia-virus-nonpermissive cells to isolate and/or purify the recombinant paramyxovirus, while codon optimization of the bacteriophage T7 gene significantly improves T7 expression and viral rescue (46). Thus, our hammerhead ribozyme design strategy, in combination with our codon-optimized T7 polymerase, resulted in a highly efficient and robust rescue system that allowed for the recovery of recombinant NiV and HeV directly from transfected producer cells without the need for blind passaging or the addition of permissive cells for amplification of the rescued virus. These improvements are likely applicable not only to henipavirus

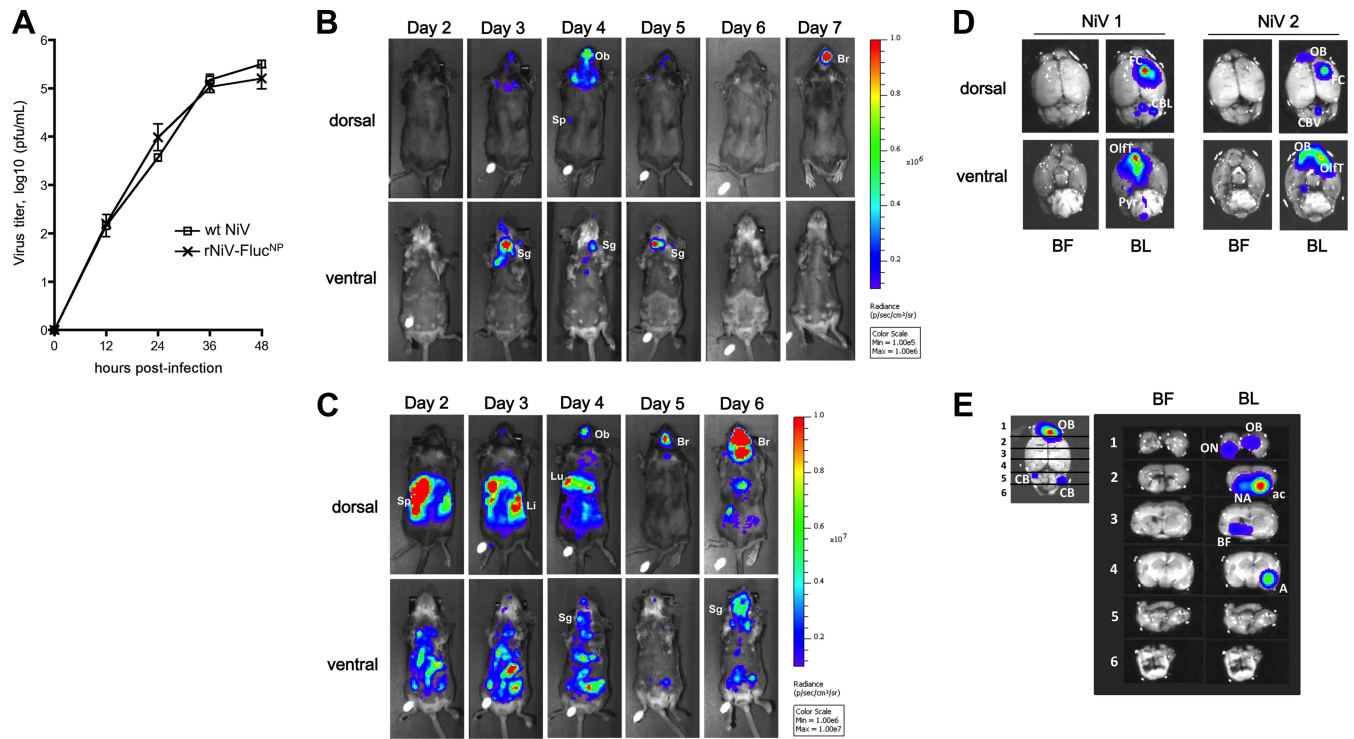


FIG 5 Fluc-expressing rNiV allows real-time monitoring of virus replication and spread in the IFNAR KO mouse. (A) HUVECs were infected with the indicated viruses at an MOI of 0.1, and the growth kinetics were monitored as described in Materials and Methods. Error bars represent standard deviations for triplicate samples. Two-way ANOVA revealed no significant difference between the two viruses ($P > 0.05$). (B and C) Groups of four IFNAR KO mice each were infected with rNiV-Fluc^{NP} via the i.n. (8×10^4 PFU/animal) (B) or i.p. (8×10^5 PFU/animal) (C) route. Infected animals were imaged at the indicated time points as described in Materials and Methods. One representative female mouse is shown for each inoculation route. The data are displayed as radiance (bioluminescence intensity) on a rainbow log scale with a range of 1×10^5 (blue) to 1×10^6 (red) photons/s/cm²/steradian for the i.n.-infected mouse and 1×10^6 to 1×10^7 photons/s/cm²/steradian for the i.p.-infected mouse. Organs with positive bioluminescence signals are labeled as follows: Br, brain; Li, liver; Lu, lung; Ob, olfactory bulb; Sg, salivary gland; Sp, spleen. (D) *Ex vivo* imaging of fresh brains from two moribund i.p.-infected mice at day 8 postinfection (identified as NiV 1 and NiV 2). BF, bright-field mode; BL, bioluminescence mode. Brain substructures with positive bioluminescence signals are labeled as follows: CBL, cerebellum, lateral hemisphere; CBV, cerebellar vermis; FC, frontal cortex; OB, olfactory bulb; OlfT, olfactory tubercle; Pyr, pyramids. (E) Gross cross sections were prepared from a fresh brain from a moribund i.p.-infected mouse at day 6 postinfection. Each numbered section in the panel on the left, showing the entire brain, corresponds to a cross section in the panel on the right. Brain substructures with positive bioluminescence signals are labeled as follows: ac, anterior commissure; A, amygdala nuclei; BF, basal forebrain; CB, cerebellum; NA, nucleus accumbens; OB, olfactory bulb; ON, olfactory nucleus.

reverse genetics but also to the reverse genetics systems of other paramyxoviruses.

As mentioned above, NiV and HeV exhibit differential tissue tropisms and pathogenic characteristics. As a first step toward the identification of the genetic determinants of these differences between NiV and HeV in the more biologically relevant context of the live virus, we rescued an isogenic panel of rNiV-HeV chimeras in which the NiV M, F, and G genes, singly and in combination, were replaced with their HeV counterparts. All chimeras resulted in efficiently replicating viruses, highlighting the phylogenetic relatedness of NiV and HeV. The ability of HeV-M to functionally interface with the heterologous NiV N/P/L replication complex and F/G envelope glycoproteins underscores a particularly close genetic relationship between NiV and HeV, since such cross-complementation of the matrix proteins of different paramyxovirus species has generally not been examined. The M and F/H envelope genes of the peste des petits ruminants virus have also shown to be functional in the genetic background of a vaccine strain of rinderpest virus, a closely related morbillivirus (47); however, it was not the intention of that study, which used a smaller set of chimeras, to dissect the genetic determinants of budding or fusogenicity for the two morbilliviruses.

In agreement with previous observations that HeV is slower to form syncytia than NiV (18, 48, 49) and that HeV-G may bind ephrin-B2 and -B3 less efficiently than NiV-G (23, 24), our results show in the context of live recombinant virus infection that the HeV-G (attachment) glycoprotein is less fusogenic than NiV-G: all heterotypic and homotypic HeV-G-bearing chimeras (Fig. 3A and B, constructs 4 to 7) form smaller and less numerous syncytia than their isogenic heterotypic and homotypic NiV-G-bearing counterparts (Fig. 3A and B, constructs 1 to 3). This decreased fusogenicity associated with HeV-G (relative to NiV-G) might contribute, in part, to observed differences in transmissibility or tropism between HeV and NiV. We anticipate that future *in vivo* experiments with firefly luciferase-expressing chimeras (see below), including corresponding insertions of the NiV-M, -F and -G genes into recombinant HeV, will shed further light on this question. In addition, our results showing higher titers of HeV-M-bearing viruses at early time points—particularly apparent in the infections of primary hNSC-derived neurons/astrocytes (Fig. 2B)—are consistent with the faster dissemination of HeV in the hamster model once infection has taken place (19).

Our reporter insertion strategy, linking the reporter to the matrix gene via a P2A ribosomal sequence, maintained the natural

polar transcriptional gradient. Interestingly, the NiV mRNA gradient resembled the previously published HeV gradient (41), with the initial sharp attenuation in transcript levels occurring at the M-F junction. Nevertheless, the wild-type transcriptional gradient observed for our initial rNiV-mCh^M infectious clone was insufficient to confer wild-type replication (Fig. 2B and C and 4B). Insertion of EGFP between the N and P genes, corresponding to the first design described for NiV reverse genetics (36), also did not affect the transcriptional gradient (Fig. 4A), but this recombinant virus replicated similarly to wild-type NiV (Fig. 4B). Therefore, transcriptional profiling by itself is not sufficient to predict wild-type replication kinetics.

To evaluate our ability to monitor the spatial and temporal progression of viral spread *in vivo*, we used a firefly luciferase-expressing NiV in the recently established IFNAR KO mouse model (20). Intraperitoneal and i.n. infections resulted in outcomes that were consistent with the previous report by Dhondt et al. (20), but real-time bioluminescence imaging shed light on the dynamic processes of viral pathogenesis and transmission. The observation of viral replication in the respiratory and urinary tracts in moribund animals provides strong evidence for the presumed modes of henipavirus transmission via respiratory secretions and urine. The spread of luminescence in i.p.-inoculated mice suggested that despite systemic infection in the body cavity, invasion of the brain might have followed viral spread to the respiratory tract and subsequent infection of the olfactory bulb, perhaps via aerosolized virus that infected olfactory receptors. While it is possible that a breach of the blood-brain barrier was also involved, the relative contributions of these mechanisms of CNS invasion deserve further investigation. Intranasal infection, on the other hand, resulted in viral spread that was limited to the upper respiratory tract, and CNS invasion again appeared to follow replication in the olfactory bulb, likely from direct infection of olfactory neurons as a result of the route of inoculation.

Our efficient and robust henipavirus reverse genetics system will enable the generation of multiple reporter viruses that will facilitate more-refined *in vitro* and *in vivo* studies of henipavirus pathogenesis and spread than have been possible to date, as well as the evaluation of vaccines and antivirals. For example, we have designed other reporter-expressing viruses with their own unique advantages for *in vivo* studies, such as an NiV with a secreted *Gaussia* luciferase-P2A-EGFP dual-expression cassette that can be used to monitor viral load directly in tissues by bioluminescence imaging or indirectly by measuring *Gaussia* luciferase activity in serum (11). Future *in vivo* studies with these reporter constructs and recombinant henipavirus chimeras will not only reveal insights into NiV and HeV pathogenesis but also open the door to similar investigations into different NiV strains (e.g., the Malaysian strain versus the more diverse Bangladeshi strains, which also appear to differ significantly in both epidemiological and experimental contexts [50–52]) and newly discovered henipaviruses (such as Cedar virus and the African bat henipavirus Gh-M74a [4, 5]).

ACKNOWLEDGMENTS

This work was partially supported by grants from the National Institute of Allergy and Infectious Diseases (NIAID) through the Western Regional Center of Excellence for Biodefense and Emerging Infectious Disease Research to A.N.F. (U54 AI057156) and the Pacific Southwest Regional Center of Excellence for Biodefense and Emerging Infectious Diseases to B.L.

(U54 AI065359). B.L. acknowledges initial funding from NIH grants R21 AI059051, R01 AI060694, and R01 AI069317 for the genesis of this project. A.P. was supported by the Ruth L. Kirschstein National Research Service award (GM007185) at UCLA. S.M.B. was supported by a Microbial Pathogenesis training grant (T32 AI07323) at UCLA and a Host-Pathogen Interactions training grant (T32 AI007647-15) at the Icahn School of Medicine at Mount Sinai. T.E.H. was funded through a Training in Emerging Infectious Diseases and Biodefense grant (T32 AI007536) at UTMB.

We thank all members of the Lee and Freiberg labs for constructive criticism, suggestions, and support. We also thank Slobodan Paessler (UTMB) for providing the IFNAR KO mice, as well as Giulio Tagliaberta (UTMB) for advice regarding analysis of imaged *ex vivo* brains. A.P. thanks Christian Aguilera for timely technical advice.

REFERENCES

1. SEARO. 13 January 2014, access date. Surveillance and outbreak alert: Nipah virus outbreaks in the WHO South-East Asia Region. World Health Organization Regional Office for South-East Asia, New Delhi, India. http://www.searo.who.int/entity/emerging_diseases/links/nipah_virus_outbreaks_sear/en/index.html.
2. Field H, Crameri G, Kung NY, Wang LF. 2012. Ecological aspects of Hendra virus. *Curr Top Microbiol Immunol* 359:11–23. http://dx.doi.org/10.1007/82_2012_214.
3. Luby SP, Gurley ES. 2012. Epidemiology of henipavirus disease in humans. *Curr Top Microbiol Immunol* 359:25–40. http://dx.doi.org/10.1007/82_2012_207.
4. Drexler JF, Corman VM, Muller MA, Maganga GD, Vallo P, Binger T, Gloza-Rausch F, Rasche A, Yordanov S, Seebens A, Oppong S, Adu Sarkodie Y, Pongombo C, Lukashev AN, Schmidt-Chanasit J, Stocker A, Carneiro AJ, Erbar S, Maisner A, Fronhoffs F, Buettner R, Kalko EK, Kruppa T, Franke CR, Kallies R, Yandoko ER, Herrler G, Reusken C, Hassanin A, Kruger DH, Matthee S, Ulrich RG, Leroy EM, Drosten C. 2012. Bats host major mammalian paramyxoviruses. *Nat Commun* 3:796. <http://dx.doi.org/10.1038/ncomms1796>.
5. Marsh GA, de Jong C, Barr JA, Tachedjian M, Smith C, Middleton D, Yu M, Todd S, Foord AJ, Haring V, Payne J, Robinson R, Broz I, Crameri G, Field HE, Wang LF. 2012. Cedar virus: a novel henipavirus isolated from Australian bats. *PLoS Pathog* 8:e1002836. <http://dx.doi.org/10.1371/journal.ppat.1002836>.
6. Muleya W, Sasaki M, Orba Y, Ishii A, Thomas Y, Nakagawa E, Ogawa H, Hang'ombe B, Namangala B, Mweene A, Takada A, Kimura T, Sawa H. 2014. Molecular epidemiology of paramyxoviruses in frugivorous *Eidolon helvum* bats in Zambia. *J Vet Med Sci* 76:611–614. <http://dx.doi.org/10.1292/jvms.13-0518>.
7. Wu Z, Yang L, Yang F, Ren X, Jiang J, Dong J, Sun L, Zhu Y, Zhou H, Jin Q. 2014. Novel henipa-like virus, Mojiang paramyxovirus, in rats, China, 2012. *Emerg Infect Dis* 20:1064–1066. <http://dx.doi.org/10.3201/eid2006.131022>.
8. Blum LS, Khan R, Nahar N, Breiman RF. 2009. In-depth assessment of an outbreak of Nipah encephalitis with person-to-person transmission in Bangladesh: implications for prevention and control strategies. *Am J Trop Med Hyg* 80:96–102.
9. Chadha MS, Comer JA, Lowe L, Rota PA, Rollin PE, Bellini WJ, Ksiazek TG, Mishra A. 2006. Nipah virus-associated encephalitis outbreak, Siliguri, India. *Emerg Infect Dis* 12:235–240. <http://dx.doi.org/10.3201/eid1202.051247>.
10. Gurley ES, Montgomery JM, Hossain MJ, Bell M, Azad AK, Islam MR, Molla MA, Carroll DS, Ksiazek TG, Rota PA, Lowe L, Comer JA, Rollin P, Czub M, Grolla A, Feldmann H, Luby SP, Woodward JL, Breiman RF. 2007. Person-to-person transmission of Nipah virus in a Bangladeshi community. *Emerg Infect Dis* 13:1031–1037. <http://dx.doi.org/10.3201/eid1307.061128>.
11. Pernet O, Schneider BS, Beaty SM, LeBreton M, Yun TE, Park A, Zachariah TT, Bowden TA, Hitchens P, Kitchen CMR, Daszak P, Mazet J, Freiberg AN, Wolfe ND, Lee B. 18 November 2014. Evidence for henipavirus spillover into human populations in Africa. *Nat Commun* <http://dx.doi.org/10.1038/ncomms6342>.
12. Luby SP. 2013. The pandemic potential of Nipah virus. *Antiviral Res* 100:38–43. <http://dx.doi.org/10.1016/j.antiviral.2013.07.011>.
13. Wong KT, Tan CT. 2012. Clinical and pathological manifestations of

- human henipavirus infection. *Curr Top Microbiol Immunol* 359:95–104. http://dx.doi.org/10.1007/82_2012_205.
14. Pernet O, Wang YE, Lee B. 2012. Henipavirus receptor usage and tropism. *Curr Top Microbiol Immunol* 359:59–78. http://dx.doi.org/10.1007/82_2012_222.
 15. Field HE, Mackenzie JS, Daszak P. 2007. Henipaviruses: emerging paramyxoviruses associated with fruit bats. *Curr Top Microbiol Immunol* 315:133–159. http://dx.doi.org/10.1007/978-3-540-70962-6_7.
 16. Geisbert TW, Feldmann H, Broder CC. 2012. Animal challenge models of henipavirus infection and pathogenesis. *Curr Top Microbiol Immunol* 359:153–177. http://dx.doi.org/10.1007/82_2012_208.
 17. Wong KT, Ong KC. 2011. Pathology of acute henipavirus infection in humans and animals. *Patholog Res Int* 2011:567248. <http://dx.doi.org/10.4061/2011/567248>.
 18. Aljofan M, Saubern S, Meyer AG, Marsh G, Meers J, Mungall BA. 2009. Characteristics of Nipah virus and Hendra virus replication in different cell lines and their suitability for antiviral screening. *Virus Res* 142:92–99. <http://dx.doi.org/10.1016/j.virusres.2009.01.014>.
 19. Rockx B, Brining D, Kramer J, Callison J, Ebihara H, Mansfield K, Feldmann H. 2011. Clinical outcome of henipavirus infection in hamsters is determined by the route and dose of infection. *J Virol* 85:7658–7671. <http://dx.doi.org/10.1128/JVI.00473-11>.
 20. Dhondt KP, Mathieu C, Chalons M, Reynaud JM, Vallve A, Raoul H, Horvat B. 2013. Type I interferon signaling protects mice from lethal henipavirus infection. *J Infect Dis* 207:142–151. <http://dx.doi.org/10.1093/infdis/jis653>.
 21. Dups J, Middleton D, Long F, Arkinstall R, Marsh GA, Wang LF. 2014. Subclinical infection without encephalitis in mice following intranasal exposure to Nipah virus-Malaysia and Nipah virus-Bangladesh. *Virol J* 11:102. <http://dx.doi.org/10.1186/1743-422X-11-102>.
 22. Dups J, Middleton D, Yamada M, Monaghan P, Long F, Robinson R, Marsh GA, Wang LF. 2012. A new model for Hendra virus encephalitis in the mouse. *PLoS One* 7:e40308. <http://dx.doi.org/10.1371/journal.pone.0040308>.
 23. Negrete OA, Chu D, Aguilar HC, Lee B. 2007. Single amino acid changes in the Nipah and Hendra virus attachment glycoproteins distinguish ephrinB2 from ephrinB3 usage. *J Virol* 81:10804–10814. <http://dx.doi.org/10.1128/JVI.00999-07>.
 24. Bossart KN, McEachern JA, Hickey AC, Choudhry V, Dimitrov DS, Eaton BT, Wang LF. 2007. Neutralization assays for differential henipavirus serology using Bio-Plex protein array systems. *J Virol Methods* 142: 29–40. <http://dx.doi.org/10.1016/j.jviromet.2007.01.003>.
 25. Buchholz UJ, Finke S, Conzelmann KK. 1999. Generation of bovine respiratory syncytial virus (BRSV) from cDNA: BRSV NS2 is not essential for virus replication in tissue culture, and the human RSV leader region acts as a functional BRSV genome promoter. *J Virol* 73:251–259.
 26. Wu P, Tarasenko YI, Gu Y, Huang LY, Coggeshall RE, Yu Y. 2002. Region-specific generation of cholinergic neurons from fetal human neural stem cells grafted in adult rat. *Nat Neurosci* 5:1271–1278. <http://dx.doi.org/10.1038/nn974>.
 27. Price SR, Ito N, Oubridge C, Avis JM, Nagai K. 1995. Crystallization of RNA-protein complexes. I. Methods for the large-scale preparation of RNA suitable for crystallographic studies. *J Mol Biol* 249:398–408.
 28. Conaty J, Hendry P, Lockett T. 1999. Selected classes of minimised hammerhead ribozyme have very high cleavage rates at low Mg^{2+} concentration. *Nucleic Acids Res* 27:2400–2407. <http://dx.doi.org/10.1093/nar/27.11.2400>.
 29. McCall MJ, Hendry P, Mir AA, Conaty J, Brown G, Lockett TJ. 2000. Small, efficient hammerhead ribozymes. *Mol Biotechnol* 14:5–17. <http://dx.doi.org/10.1385/MB:14:1:5>.
 30. Persson T, Hartmann RK, Eckstein F. 2002. Selection of hammerhead ribozyme variants with low Mg^{2+} requirement: importance of stem-loop II. *ChemBiochem* 3:1066–1071. [http://dx.doi.org/10.1002/1439-7633\(20021104\)3:11<1066::AID-CBIC1066>3.0.CO;2-G](http://dx.doi.org/10.1002/1439-7633(20021104)3:11<1066::AID-CBIC1066>3.0.CO;2-G).
 31. Fedoruk-Wyszomirska A, Szymanski M, Wyszko E, Barciszewska MZ, Barciszewski J. 2009. Highly active low magnesium hammerhead ribozyme. *J Biochem* 145:451–459. <http://dx.doi.org/10.1093/jb/mvn182>.
 32. Burke DH, Greathouse ST. 2005. Low-magnesium, trans-cleavage activity by type III, tertiary stabilized hammerhead ribozymes with stem 1 discontinuities. *BMC Biochem* 6:14. <http://dx.doi.org/10.1186/1471-2091-6-14>.
 33. Halpin K, Bankamp B, Harcourt BH, Bellini WJ, Rota PA. 2004. Nipah virus conforms to the rule of six in a minigenome replication assay. *J Gen Virol* 85:701–707. <http://dx.doi.org/10.1099/vir.0.19685-0>.
 34. Sleeman K, Bankamp B, Hummel KB, Lo MK, Bellini WJ, Rota PA. 2008. The C, V and W proteins of Nipah virus inhibit minigenome replication. *J Gen Virol* 89:1300–1308. <http://dx.doi.org/10.1099/vir.0.83582-0>.
 35. Ciancanelli MJ, Volchkova VA, Shaw ML, Volchkov VE, Basler CF. 2009. Nipah virus sequesters inactive STAT1 in the nucleus via a P gene-encoded mechanism. *J Virol* 83:7828–7841. <http://dx.doi.org/10.1128/JVI.02610-08>.
 36. Yoneda M, Guillaume V, Ikeda F, Sakuma Y, Sato H, Wild TF, Kai C. 2006. Establishment of a Nipah virus rescue system. *Proc Natl Acad Sci U S A* 103:16508–16513. <http://dx.doi.org/10.1073/pnas.0606972103>.
 37. Wang YE, Park A, Lake M, Pentecost M, Torres B, Yun TE, Wolf MC, Holbrook MK, Freiberg AN, Lee B. 2010. Ubiquitin-regulated nuclear-cytoplasmic trafficking of the Nipah virus matrix protein is important for viral budding. *PLoS Pathog* 6:e1001186. <http://dx.doi.org/10.1371/journal.ppat.1001186>.
 38. Yun NE, Poussard AL, Seregin AV, Walker AG, Smith JK, Aronson JF, Smith JN, Soong L, Paessler S. 2012. Functional interferon system is required for clearance of Lassa virus. *J Virol* 86:3389–3392. <http://dx.doi.org/10.1128/JVI.06284-11>.
 39. Lo MK, Peeples ME, Bellini WJ, Nichol ST, Rota PA, Spiropoulou CF. 2012. Distinct and overlapping roles of Nipah virus P gene products in modulating the human endothelial cell antiviral response. *PLoS One* 7:e47790. <http://dx.doi.org/10.1371/journal.pone.0047790>.
 40. Bossart KN, Wang LF, Flora MN, Chua KB, Lam SK, Eaton BT, Broder CC. 2002. Membrane fusion tropism and heterotypic functional activities of the Nipah virus and Hendra virus envelope glycoproteins. *J Virol* 76: 11186–11198. <http://dx.doi.org/10.1128/JVI.76.22.11186-11198.2002>.
 41. Wright PJ, Cramer G, Eaton BT. 2005. RNA synthesis during infection by Hendra virus: an examination by quantitative real-time PCR of RNA accumulation, the effect of ribavirin and the attenuation of transcription. *Arch Virol* 150:521–532. <http://dx.doi.org/10.1007/s00705-004-0417-5>.
 42. Amano O, Mizobe K, Bando Y, Sakiyama K. 2012. Anatomy and histology of rodent and human major salivary glands: overview of the Japan Salivary Gland Society-sponsored workshop. *Acta Histochem Cytochem* 45:241–250. <http://dx.doi.org/10.1267/ahc.12013>.
 43. Conzelmann KK. 2004. Reverse genetics of *Mononegavirales*. *Curr Top Microbiol Immunol* 283:1–41. http://dx.doi.org/10.1007/978-3-662-06099-5_1.
 44. Ghanem A, Kern A, Conzelmann KK. 2012. Significantly improved rescue of rabies virus from cDNA plasmids. *Eur J Cell Biol* 91:10–16. <http://dx.doi.org/10.1016/j.ejcb.2011.01.008>.
 45. Eckstein F, Kore AR, Nakamaye KL. 2001. In vitro selection of hammerhead ribozyme sequence variants. *ChemBiochem* 2:629–635. [http://dx.doi.org/10.1002/1439-7633\(20010903\)2:9<629::AID-CBIC629>3.0.CO;2-3](http://dx.doi.org/10.1002/1439-7633(20010903)2:9<629::AID-CBIC629>3.0.CO;2-3).
 46. Beaty SM, Park A, Yun T, Pernet O, Vigant F, Allen A, Wang Y, Lyons M, Rennick LJ, McQueen NL, Freiberg AN, Elankumaran S, Duprex WP, Lee B. 2013. Efficient rescue and reverse genetics of viruses from all *Paramyxovirinae* genera without the use of vaccinia-driven T7 polymerase, p 79. XV Int Conf Negative Strand Viruses, Granada, Spain.
 47. Mahapatra M, Parida S, Baron MD, Barrett T. 2006. Matrix protein and glycoproteins F and H of Peste-des-petits-ruminants virus function better as a homologous complex. *J Gen Virol* 87:2021–2029. <http://dx.doi.org/10.1099/vir.0.81721-0>.
 48. Wang LF, Daniels P. 2012. Diagnosis of henipavirus infection: current capabilities and future directions. *Curr Top Microbiol Immunol* 359: 179–196. http://dx.doi.org/10.1007/82_2012_215.
 49. Escaffre O, Borisevich V, Carmical JR, Prusak D, Prescott J, Feldmann H, Rockx B. 2013. Henipavirus pathogenesis in human respiratory epithelial cells. *J Virol* 87:3284–3294. <http://dx.doi.org/10.1128/JVI.02576-12>.
 50. Luby SP, Gurley ES, Hossain MJ. 2009. Transmission of human infection with Nipah virus. *Clin Infect Dis* 49:1743–1748. <http://dx.doi.org/10.1086/647951>.
 51. Clayton BA, Middleton D, Bergfeld J, Haining J, Arkinstall R, Wang L, Marsh GA. 2012. Transmission routes for Nipah virus from Malaysia and Bangladesh. *Emerg Infect Dis* 18:1983–1993. <http://dx.doi.org/10.3201/eid1812.120875>.
 52. DeBuysscher BL, de Wit E, Munster VJ, Scott D, Feldmann H, Prescott J. 2013. Comparison of the pathogenicity of Nipah virus isolates from Bangladesh and Malaysia in the Syrian hamster. *PLoS Negl Trop Dis* 7:e2024. <http://dx.doi.org/10.1371/journal.pntd.0002024>.